



# Elastoplastic Damage Modeling of Rock Spalling/Failure Induced by a Filled Flaw Using the Material Point Method (MPM)

Shu-Gang Ai<sup>1</sup> · Ke Gao<sup>1,2</sup>

Received: 11 October 2022 / Accepted: 7 February 2023

© The Author(s), under exclusive licence to Springer-Verlag GmbH Austria, part of Springer Nature 2023

## Abstract

The spalling/failure of rocks often occurs at the underground opening surface during excavation activities, which may also be seriously affected by geological conditions such as joints and cracks. The nearby joints are usually filled with materials such as mortar or concrete to improve the stability of the opening surrounding rocks. To study the rock spalling/failure induced by a filled flaw, we adopt the weighted least squares material point method framework where a coupled Drucker–Prager plasticity and Grady–Kipp damage model is used to capture the mixed tensile-shear failure, and a particle-to-surface contact formulation is employed to model the contact interaction between the filled flaw and surrounding rocks. The framework is benchmarked using a series of cases involving circular opening, penny-shaped crack, and crack propagation, which shows a good agreement between the analytical, experimental, and numerical results. Simulations of plane strain compression tests for an arch-shaped tunnel opening under different geological conditions are also performed, where the rock spalling process is numerically reproduced by the sequential appearance of multiple cracks initiated from the opening surface. We show that the filling exacerbates the spalling at the tunnel left spandrel and induces new mixed shear-tensile cracks connected from the flaw toe to the tunnel corner, and massive collapse could occur at the tunnel left waist when the area formed by the spalling and band failure at the tunnel left spandrel and corner is connected to the filler. Our results suggest that our proposed MPM framework is an attractive alternative for the study of rock spalling/failure for underground openings.

## Highlights

- A coupled plasticity-damage MPM framework considering particle-to-surface contact is constructed.
- The effectiveness of the constructed MPM framework for rock spalling/failure simulation is confirmed.
- Spalling is reproduced by the sequential appearance of multiple cracks starting at the opening surface.
- The filling of nearby open flaws could exacerbate the spalling and cause even massive collapse.

**Keywords** Rock spalling/failure · Filled flaw · Elastoplastic damage · Material point method (MPM) · Contact interplay

## 1 Introduction

The surface instability or failure of rocks adjacent to a free surface of underground openings such as deep tunnels or boreholes, particularly when subjected to high-stress conditions, is often manifested as a spalling phenomenon. The rock spalling is formed by the cracks' initiation, propagation, and coalescence, and the detachment of thin rock pieces near free surfaces. The mechanical processes depend on not only the high in situ stress field (Jacobsson et al. 2015; Vardoulakis and Papanastasiou 1988) but also the complex geological conditions such as joints, bedding planes, faults, and natural

---

✉ Ke Gao  
gaok@sustech.edu.cn

<sup>1</sup> Department of Earth and Space Sciences, Southern University of Science and Technology, Shenzhen, Guangdong 518055, China

<sup>2</sup> Guangdong Provincial Key Laboratory of Geophysical High-Resolution Imaging Technology, Southern University of Science and Technology, Shenzhen, Guangdong 518055, China

weak interlayers (Huang et al. 2013; Mazaira and Konicek 2015; Pan et al. 2020b; Zhuang et al. 2014). It was reported that the sudden slip of fault near the tunnel under excavation could trigger a series of rock burst events, then resulting in an instantaneous spalling/failure at the tunnel surface, and consequently leading to a geological disaster (Lee and Kim 2003; Zhang et al. 2012). Therefore, understanding the occurrence and formation of rock spalling/failure during excavation activities is critical to the design and safe construction of underground openings, especially when there exist nearby faults.

There have been extensive experimental and theoretical studies on the spalling/failure of rock materials (Gong et al. 2018; Jacobsson et al. 2015; Kao et al. 2016; Mazaira and Konicek 2015; Papamichos et al. 1994; Tarokh et al. 2016b). Much of the work has concentrated on identifying key factors influencing surface spalling behavior and has highlighted the importance of the geological environments of rock masses around an underground opening. Jeon et al. (2004) carried out scaled model tests to study the effect of faults, weak planes, and grouting on tunnel stability and observed that the existence of nearby geological discontinuities furthers the surface deformation of tunnel side walls. The failure pattern of the tunnel crossing through a weak interlayer was explored in the same way where the interlayer's location, dip, and thickness were considered (Huang et al. 2013). Song et al. (2018) adopted the 3D printing technology to establish fault-tunnel physical models to simulate nearby fault-induced tunnel spalling and collapse more accurately. As far as discontinuous faults or flaws are concerned, research is mostly focused on open and closed fractures without artificial fillings. To improve the surrounding rock stability, however, grouting and shotcrete technology are often applied where the nearby flaws are filled with mortar, concrete, etc. to reinforce their mechanical resistance to further rupture propagation. Zhuang et al. (2014) performed uniaxial compression tests to investigate the influence of filling materials on the crack behavior and concluded that the filling of flaws changes the crack initiation stress and angle. In addition, the crack process and failure pattern of sandstone for cases with different filling materials and flaw inclination angles were also examined (Miao et al. 2018). Moreover, Pan et al. (2020b) experimentally analyzed the spalling process of the hard rock tunnel nearby a flaw filled with different materials and found the tangential stress concentration induced by the pre-existing flaw induces the spalling/failure. Compared to the above experiments, however, numerical simulations can provide complementary information such as the accurate stress distribution and strain evolution for further insights into the spalling/failure.

The rock spalling/failure under unfavorable geological conditions was modeled and investigated using various numerical methods. Zubelewicz and Mroz (1983) used the

finite-element method (FEM) to study the unstable dynamic failure of rock bursts. Shou (2000) developed a hybrid boundary element method (BEM) to analyze the nonlinear behavior of weak planes near underground excavations. Lee and Kim (2003) implemented a hybrid FEM–BEM technique for evaluating the effect of fault zones on tunnel movement during the construction process. Jiao et al. (2012) employed the discontinuous deformation analysis (DDA) method to simulate the fragmentation and collapse of an opening surrounded by jointed sandstone. The surface spalling and crack propagation were also successfully modeled by the discrete-element method (DEM) (Fakhimi et al. 2002; Sagong et al. 2011; Tarokh et al. 2016a) and the numerical manifold method (NMM) (Li et al. 2018; Wu et al. 2018; Yang et al. 2016). In addition, Lisjak (2013) captured the formation of an excavation damage zone around an underground opening based on the combined finite–discrete-element method (FDEM). It was observed that with the development of advanced computational methods used for modeling fracture behavior, numerical simulations have been playing a crucial role in the study of rock surface spalling/failure. In general, however, the effectiveness of numerical techniques always needs to be verified and illustrated through comparison with physical experimental results, such as that done in References (Huang et al. 2013; Jeon et al. 2004; Zhuang et al. 2014). Recently, to reveal the intrinsic mechanism that controls tunnel spalling/failure, the elastoplastic cellular automaton (EPCA) code was applied in examining the stress concentration in the surrounding rocks while the physical experiments were conducted (Pan et al. 2020b). We notice that the opening peak-post large or discontinuous deformation and the contact interaction between filled flaw and sandstone were still not modeled, which inevitably affects the understanding of rock spalling/failure induced by a nearby filled flaw.

The challenge of accurately modeling rock spalling/failure mainly lies in the choice and implementation of a deformation regime and constitutive model of rock under loading and unloading conditions. In addition to the numerical methods mentioned before, the material point method (MPM) has the potential to achieve large or discontinuous deformation in the fracture process due to the continual grid resetting therein. The MPM has been successfully applied in the context of solid mechanics (Sulsky et al. 1995), fluid mechanics (York et al. 2000), soil mechanics (Bandara and Soga 2015; Hu et al. 2021; Liu et al. 2020), computer graphics (Klár et al. 2016), fracture mechanics (Hu et al. 2022; Nairn 2018), etc. The method will probably help obtain the whole spalling process from continuous to discontinuous deformation. On the other hand, the focus is how to accurately capture both shear and tensile fracture behavior in rock spalling/failure. Recently, the coupled Drucker–Prager (DP) plasticity and Grady–Kipp (GK) damage model has

proved successful in modeling mixed-mode fracture in the smoothed particle hydrodynamics (SPH) framework (Douillet-Grellier et al. 2016a). Following this, the proposed model was first incorporated into the MPM framework to simulate the failure of aggregate materials (Raymond et al. 2019) and then the shearing of polycrystalline materials (Raymond et al. 2021). For underground openings nearby a filled flaw, however, one needs to introduce a contact formulation in the coupled DP and GK MPM framework to explore the interplay between opening surface spalling and filler-induced pre-crack propagation.

This study aims to develop a coupled plasticity-damage MPM framework considering contact interaction between filled flaws and surrounding rocks for the numerical study of rock spalling/failure induced by a filled flaw. We first provide a detailed description of the implementation of the MPM (Sulsky et al. 1995) using the weighted least squares (WLS) approximation (Hu et al. 2018), where the frictional contact modeling is resolved with the penalty-based particle-to-surface (PTS) contact algorithm (Nakamura et al. 2021). The coupled DP plasticity and GK damage model (Douillet-Grellier et al. 2016a; Raymond et al. 2019) is also presented. Then, we perform simulations of benchmark problems including circular opening, penny-shaped crack, and dynamic crack propagation under uniaxial compression to illustrate the effectiveness of the MPM framework built in this study. Finally, we analyze the failure patterns and profiles by tracking the spalling process of tunnels nearby a filled flaw and reveal the influence of the filled flaw on spalling/failure of the tunnel opening.

## 2 MPM Using the WLS Approximation

### 2.1 Governing Equations

We begin with the governing equations of the conservations of mass and momentum considering an updated Lagrangian framework, which are given as

$$\frac{D\rho}{Dt} + \rho \nabla \cdot \mathbf{v} = 0, \quad (1)$$

$$\rho \frac{D\mathbf{v}}{Dt} = \nabla \cdot \boldsymbol{\sigma} + \rho \mathbf{g}, \quad (2)$$

where  $\rho$  is the mass density;  $\mathbf{v}$  is the velocity;  $\boldsymbol{\sigma}$  is the Cauchy stress;  $\mathbf{g}$  is the gravitational acceleration (9.81 m/s<sup>2</sup>);  $D\varphi/Dt = \partial\varphi/\partial t + \mathbf{v} \cdot \nabla\varphi$  denotes the material derivative of any field quantity  $\varphi(\mathbf{x}, t)$ . Before discretizing and solving the partial differential Eq. (2) via MPM, its strong form has to be transformed into a weak integral form on the problem domain  $\Omega$  as in FEM (de Souza Neto et al. 2011). Thus,

Eq. (2) is sequentially multiplied by an arbitrary test function  $\mathbf{w}$  (i.e., virtual displacement field), integrated by parts, and reformulated by carrying out the divergence theorem and applying the boundary conditions as

$$\int_{\Omega} (\rho \dot{\mathbf{v}} \cdot \mathbf{w}) d\Omega = \int_{\Omega} (\boldsymbol{\sigma} : \nabla \mathbf{w}) d\Omega + \int_{\Omega} (\rho \mathbf{g} \cdot \mathbf{w}) d\Omega + \int_{\partial\Omega_t} (\mathbf{t} \cdot \mathbf{w}) d\partial\Omega_t, \quad (3)$$

where  $\mathbf{t} = \boldsymbol{\sigma} \mathbf{n}$  denotes the traction boundary condition with  $\mathbf{n}$  indicating the unit normal to the domain boundary  $\partial\Omega_t$ .

### 2.2 MPM Discretization

The MPM discretizes the problem domain into a set of Lagrangian material point particles, then interpolated at the connected nodes, and finally moves through a fixed Eulerian background grid where the solution is performed. Through the discretization, the problem domain  $\Omega$  is additively decomposed into the corresponding particle domain contributions where each particle represents a finite Lagrangian domain  $\Omega_p$  whose properties (e.g., mass  $m_p$ , volume  $V_p$ , velocity  $\mathbf{v}_p$  and its gradient  $\nabla \mathbf{v}_p$ , Cauchy stress  $\boldsymbol{\sigma}_p$  and its related material variables, position  $\mathbf{x}_p$ ) are being tracked (Burghardt et al. 2012), which is expressed as

$$\Omega(\mathbf{x}, t) = \sum_{p=1}^{N_p} \Omega_p \delta(\mathbf{x} - \mathbf{x}_p), \quad (4)$$

where  $\mathbf{x}_p$  is the position vector of material particle  $p$ ;  $N_p$  is the total number of material particles;  $\delta$  is the Dirac delta function. Substituting Eq. (4) back into Eq. (3), the following global discrete relation is established:

$$\begin{aligned} \sum_{p=1}^{N_p} \int_{\Omega_p} (\rho \dot{\mathbf{v}} \cdot \mathbf{w}) d\Omega_p &= \sum_{p=1}^{N_p} \int_{\Omega_p} (\boldsymbol{\sigma} : \nabla \mathbf{w}) d\Omega_p \\ &+ \sum_{p=1}^{N_p} \int_{\Omega_p} (\rho \mathbf{g} \cdot \mathbf{w}) d\Omega_p \\ &+ \sum_{p=1}^{N_p} \int_{\partial\Omega_{tp}} (\mathbf{t} \cdot \mathbf{w}) d\partial\Omega_{tp} \end{aligned} \quad (5)$$

Same as that in the FEM, the field variables such as  $\mathbf{v}_p$  and  $\nabla \mathbf{v}_p$  in the MPM are approximated by given shape functions that interpolate nodal values, i.e.,

$$\mathbf{v}_p = \sum_{i=1}^{N_i} \psi_i(\mathbf{x}_p) \mathbf{v}_i, \quad (6)$$

$$\nabla \mathbf{v}_p = \sum_{i=1}^{N_i} \mathbf{v}_i \otimes \nabla \psi_i(\mathbf{x}_p), \quad (7)$$

where  $N_i$  is the total number of grid nodes and  $\psi_i(\mathbf{x}_p)$  is the interpolation functions evaluated at particle  $p$ . This allows those integrals in Eq. (5) to be locally approximated such that the discretized problem can be linearly solved. In this study, the WLS approximation is adopted to generate the specific shape functions, which can effectively resolve the inconsistent transfers of physical quantities when considering frictional contact (Hu et al. 2018; Nakamura et al. 2021). For a given  $\mathbf{x}_p$ , we construct its local approximation using a polynomial least squares method such that a target field  $h_p(\mathbf{x})$  at any position  $\mathbf{x}$  around  $\mathbf{x}_p$  can be expressed as

$$h_p(\mathbf{x}) = \mathbf{p}^T(\mathbf{x} - \mathbf{x}_p)\mathbf{c}(\mathbf{x}_p), \tag{8}$$

$$\mathbf{c}(\mathbf{x}_p) = \mathbf{M}^{-1}(\mathbf{x}_p) \sum_{i=1}^{N_i} w_i(\mathbf{x}_p)\mathbf{p}_i(\mathbf{x}_i - \mathbf{x}_p)h_i(\mathbf{x}_p), \tag{9}$$

$$\mathbf{M}(\mathbf{x}_p) = \sum_{i=1}^{N_i} w_i(\mathbf{x}_p)\mathbf{p}_i^T(\mathbf{x}_i - \mathbf{x}_p)\mathbf{p}_i(\mathbf{x}_i - \mathbf{x}_p), \tag{10}$$

$$J_p(\mathbf{c}) = \sum_{i=1}^{N_i} w_i(\mathbf{x}_p)[\mathbf{p}_i^T(\mathbf{x}_i - \mathbf{x}_p)\mathbf{c}(\mathbf{x}_p) - h_i(\mathbf{x}_p)]^2, \tag{11}$$

where  $\mathbf{p}(\mathbf{x}) = [1, x, y, z]^T$  denotes the selected complete polynomial basis in three dimensions (3D);  $\mathbf{c}(\mathbf{x}_p)$  is the coefficient vector calculated using the WLS minimizing the functional defined by  $J_p(\mathbf{c})$ ;  $w_i(\mathbf{x}_p)$  is the localized weighting function that is chosen to be cubic B-splines in this study (Fig. 1a). The weight function and its kernel are defined as (Klár et al. 2016)

$$w_i(\mathbf{x}) = \tilde{w}\left(\frac{x-x_i}{l}\right)\tilde{w}\left(\frac{y-y_i}{l}\right)\tilde{w}\left(\frac{z-z_i}{l}\right), \tag{12}$$

$$\tilde{w}(x) = \begin{cases} \frac{1}{2}|x|^3 - |x|^2 + \frac{2}{3} & 0 \leq |x| < 1 \\ \frac{1}{6}(2 - |x|)^3 & 1 \leq |x| < 2 \\ 0 & 2 \leq |x| \end{cases}, \tag{13}$$

where  $l$  is the grid spacing. By introducing the shape functions  $\psi_i(\mathbf{x}_p)$ , Eq. (8) can be rewritten as

$$h_p(\mathbf{x}) = \sum_{i=1}^{N_i} \psi_i(\mathbf{x})h_i(\mathbf{x}_p), \tag{14}$$

where

$$\psi_i(\mathbf{x}) = w_i(\mathbf{x}_p)\mathbf{p}_i^T(\mathbf{x} - \mathbf{x}_p)\mathbf{M}^{-1}(\mathbf{x}_p)\mathbf{p}_i(\mathbf{x}_i - \mathbf{x}_p). \tag{15}$$

Subsequently, using Shepard’s method (Shepard 1968), the local approximation  $h_p(\mathbf{x})$  for a given  $\mathbf{x}_p$  is extended into the global approximation  $h(\mathbf{x})$ , which is defined as

$$h(\mathbf{x}) = \sum_{p=1}^{N_p} \xi_p(\mathbf{x})h_p(\mathbf{x}), \tag{16}$$

$$\xi_p(\mathbf{x}) = \frac{w(\mathbf{x}_p - \mathbf{x})m_p}{\sum_{q=1}^{N_q} w(\mathbf{x}_q - \mathbf{x})m_q}. \tag{17}$$

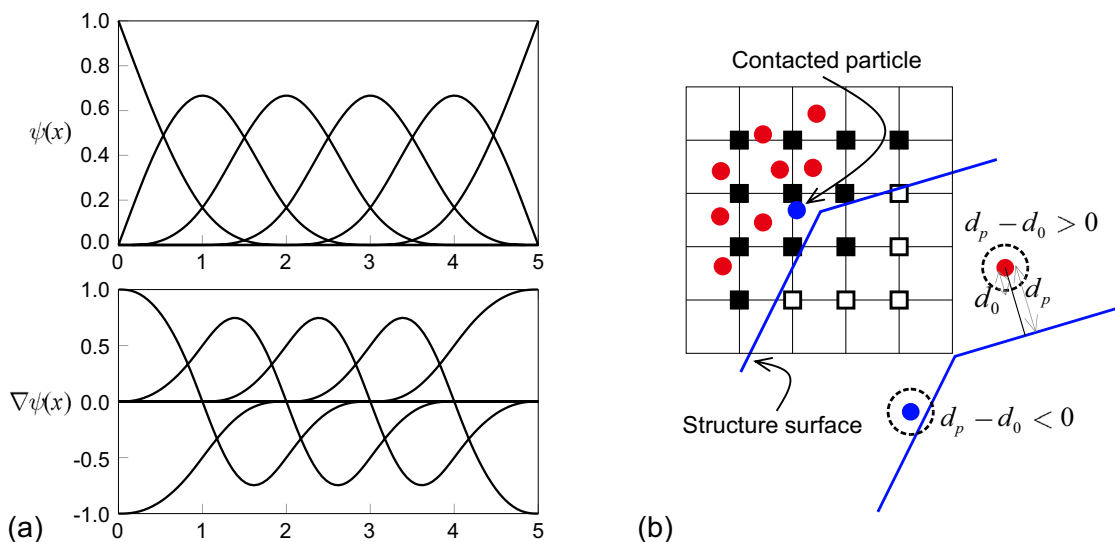


**Fig. 1** **a** Cubic B-splines weighting functions and their gradient and **b** PTS contact criterion (Nakamura et al. 2021), where the open and solid squares denote the active and inactive grid nodes when two bod-

ies are in contact, and the open and solid circles denote the contacted and uncontacted material points, respectively

Eventually taking the well-defined WLS approximation, the final equation discretized by the MPM can be obtained by substituting Eqs. (6) and (7) into Eq. (5), which yields

$$\sum_{j=1}^{N_j} M_{ij} \dot{\mathbf{v}}_j = \mathbf{f}_i^{\text{int}} + \mathbf{f}_i^{\text{ext}}, \quad (18)$$

$$M_{ij} = \sum_{p=1}^{N_p} m_p \psi_i(\mathbf{x}_p) \psi_j(\mathbf{x}_p), \quad (19)$$

$$m_i = \sum_{p=1}^{N_p} m_p \psi_i(\mathbf{x}_p), \quad (20)$$

$$\mathbf{f}_i^{\text{int}} = \sum_{p=1}^{N_p} V_p \boldsymbol{\sigma}_p \nabla \psi_i(\mathbf{x}_p), \quad (21)$$

$$\mathbf{f}_i^{\text{ext}} = \sum_{p=1}^{N_p} \psi_i(\mathbf{x}_p) m_p \mathbf{g} + \int_{\partial\Omega_i} \psi_i(\mathbf{x}) \mathbf{t} d\Omega_i, \quad (22)$$

where  $M_{ij}$  is the consistent mass matrix and usually reduced to the lumped mass matrix  $m_i$  through the justification of the special mass lumping technique from Hinton et al. (1976) that not only ensures the positive definiteness of the mass matrix (Li and Liu 2007) but also avoids the expensive matrix inversion (Bardenhagen and Kober 2004). Note that explicit time integration is used to solve the MPM equations for simulating quasi-static or slow-process problems in this study. Thus, the time step is required to be small enough to satisfy the stability condition and determined by  $\Delta t \leq l / (v_c + \|\mathbf{v}\|)$  where  $v_c$  being the characteristic P-wave velocity.

### 2.3 PTS Contact

We employ the PTS contact formulation proposed by Wang and Chan (2014) to simulate the frictional contact interaction between the MPM domain (particles) and structure (surfaces). With an emphasis on investigating the effect of filling material on rock spalling of opening, the rigid structure representing the domain occupied by the filling material is used in this study. This algorithm possibly allows a material particle to partially penetrate the rigid structure, where a parameter factor  $\chi$  is introduced to define the amount of residual penetration ( $0 \leq \chi < 1$  where  $\chi = 0$  implies zero penetration). Thus, the normal contact force is given by

$$\mathbf{f}_i^{\text{nor}} = \begin{cases} -\sum_{p=1}^{N_p} \psi_i(\mathbf{x}_p) (1 - \chi) \kappa_p^{\text{nor}} \mathbf{d}_p^{\text{nor}} & d_p - d_0 < 0 \\ 0 & d_p - d_0 \geq 0 \end{cases}, \quad (23)$$

where the value of  $(d_p - d_0)$  denotes the contact distance from the particle to the surface and  $d_p - d_0 < 0$  when contact occurs, as shown in Fig. 1b;  $\mathbf{d}_p^{\text{nor}} = (d_p - d_0) \mathbf{n}_p$  denotes the normal contact distance vector related to the unit normal  $\mathbf{n}_p$  from particle to surface;  $\kappa_p^{\text{nor}} = 2m_p / (\Delta t)^2$  is the penalty parameter derived by Newton's second law of motion. On the other hand, the tangential or frictional contact force is given as

$$\mathbf{f}_i^{\text{tan}} = \begin{cases} f_i^{\text{tan(max)}} \mathbf{n}_i^{\text{stick}} & \|\mathbf{f}_i^{\text{stick}}\| \geq f_i^{\text{tan(max)}} \\ \mathbf{f}_i^{\text{stick}} & \|\mathbf{f}_i^{\text{stick}}\| < f_i^{\text{tan(max)}} \end{cases}. \quad (24)$$

In the equation above,  $f_i^{\text{tan(max)}} = \mu_{\text{con}} \|\mathbf{f}_i^{\text{nor}}\| + A_{\text{con}} c_{\text{con}}$  denotes the admissible maximum frictional contact force where  $\mu_{\text{con}}$  and  $c_{\text{con}}$  are the frictional coefficient and cohesion;  $A_{\text{con}}$  is the contacted area at node  $i$  that is evaluated as the value of grid spacing  $l$  in 2D or the area occupied by node  $i$  in 3D (i.e., grid cell area), which is constant owing to the fixed and regular background grid used in this study;  $\mathbf{n}_i^{\text{stick}} = \mathbf{f}_i^{\text{stick}} / \|\mathbf{f}_i^{\text{stick}}\|$  denotes the unit tangential vector;  $\mathbf{f}_i^{\text{stick}} = -m_i \tilde{\mathbf{v}}_i^{\text{tan}} / \Delta t$  denotes the tangential contact force calculated by assuming no sliding between particle and surface where  $\tilde{\mathbf{v}}_i^{\text{tan}}$  is the tangential component of relative velocity between particle and surface and can be obtained as

$$\tilde{\mathbf{v}}_i^{\text{tan}} = \tilde{\mathbf{v}}_i - (\tilde{\mathbf{v}}_i \cdot \mathbf{n}_i^{\text{nor}}) \mathbf{n}_i^{\text{nor}}, \quad (25)$$

$$\tilde{\mathbf{v}}_i = \sum_{p=1}^{N_p} \xi_p(\mathbf{x}_i) \mathbf{v}_i(\mathbf{x}_i) - \sum_{p=1}^{N_p} \xi_p(\mathbf{x}_i) \mathbf{v}_i^{\text{rigid}}(\mathbf{x}_i), \quad (26)$$

where  $\mathbf{n}_i^{\text{nor}} = \mathbf{f}_i^{\text{nor}} / \|\mathbf{f}_i^{\text{nor}}\|$  denotes the unit normal vector;  $\mathbf{v}_i(\mathbf{x}_i)$  is the nodal velocity at the active grid node  $\mathbf{x}_i$ ;  $\mathbf{v}_i^{\text{rigid}}(\mathbf{x}_i)$  is the velocity at the position  $\mathbf{x}_i$ , calculated by the distance from  $\mathbf{x}_i$  to the center of a rigid body, the velocity, and the rotational moment of the rigid body. Note that before the PTS contact calculation, the initial distance of particle used for the contact detection  $d_0$  and the parameter factor  $\chi$  controlling residual penetration should be given. Lately, the PTS contact algorithm has been extended to the MPM framework, and more details of implementation were provided by Nakamura et al. (2021).

## 2.4 Coupled DP Plasticity and GK Damage Model

We pursue the coupled DP plasticity and GK damage model to capture rock spalling/failure induced by the filling of a nearby flaw in the framework of weighted least squares material point method (WLS-MPM) with the PTS contact formulation. The constitutive calculation consists of three steps, namely an elastic trial step, a plastic corrector step, and a damage corrector step. First, the elastic trial stress is calculated using the generalized Hooke's law where the incremental strain is imposed via an additive volumetric–deviatoric decomposition, which yields

$$\dot{\boldsymbol{\sigma}} = 2G\dot{\boldsymbol{\epsilon}}^{\text{dev}} + K\dot{\boldsymbol{\epsilon}}^{\text{vol}}, \quad (27)$$

$$\dot{\boldsymbol{\epsilon}} = \underbrace{\dot{\boldsymbol{\epsilon}} - \text{tr}(\dot{\boldsymbol{\epsilon}})\mathbf{I}/3}_{\dot{\boldsymbol{\epsilon}}^{\text{dev}}} + \underbrace{\text{tr}(\dot{\boldsymbol{\epsilon}})\mathbf{I}/3}_{\dot{\boldsymbol{\epsilon}}^{\text{vol}}}, \quad (28)$$

$$\dot{\boldsymbol{\epsilon}} = \frac{1}{2}[\nabla\mathbf{v} + (\nabla\mathbf{v})^T], \quad (29)$$

where  $G$  and  $K$  are the shear and bulk moduli, respectively. Then, substituting the elastic trial stress into the DP yield function, the stress state is decided. If the trial state is still in the elastic regime, the trial state is the true state and the constitutive calculation is terminated. Otherwise, the DP plastic corrector step is performed to return the trial stress to the yield surface. Afterward, the updated stress state is tested for tensile failure and then corrected using the GK damage model. In the following, we will briefly describe the DP plasticity and GK damage model.

### 2.4.1 DP Plasticity

The DP yield criterion is used to predict the shear failure of rock from its trial elastic stress state, which is defined as (Zhang et al. 2016)

$$F_p(\boldsymbol{\tau}, \sigma_m) = \tau + q_\phi \sigma_m - \bar{k}_\phi c_{\text{mat}}, \quad (30)$$

where  $\tau = \sqrt{J_2(\boldsymbol{\sigma})}$  is the effective shear stress;  $\sigma_m = I_1(\boldsymbol{\sigma})/3$  is the mean stress;  $c_{\text{mat}}$  is the cohesion of rock material. We adopt the DP yield surface passing through the outer apexes of the Mohr–Coulomb (MC) yield surface in the  $\pi$ -plane. Thus, the parameters  $q_\phi$  and  $\bar{k}_\phi$  are given by

$$q_\phi = \frac{6 \sin \phi_{\text{mat}}}{\sqrt{3}(3 - \sin \phi_{\text{mat}})}, \quad \bar{k}_\phi = \frac{6 \cos \phi_{\text{mat}}}{\sqrt{3}(3 - \sin \phi_{\text{mat}})}, \quad (31)$$

where  $\phi_{\text{mat}}$  is the friction angle of rock material. Meanwhile, a non-associated rule is applied to consider the dilatancy of frictional materials, resulting in the plastic potential function related to the dilatancy angle  $\psi_{\text{mat}}$  and defined as

$$\tilde{F}_p(\boldsymbol{\tau}, \sigma_m) = \tau + q_\psi \sigma_m, \quad (32)$$

$$q_\psi = \frac{6 \sin \psi_{\text{mat}}}{\sqrt{3}(3 - \sin \psi_{\text{mat}})}. \quad (33)$$

In addition, the associative isotropic strain softening given by Deb and Pramanik (2013) is considered by letting  $c_{\text{mat}}$  be a piecewise linear function of the accumulated plastic strain  $\bar{\epsilon}_p$ , which is expressed as

$$c_{\text{mat}}(\bar{\epsilon}_p) = \begin{cases} c_{\text{mat}(0)}(1 - \bar{\epsilon}_p/\bar{\epsilon}_{p(\text{crit})}) & c_{\text{mat}}(\bar{\epsilon}_p) \geq 0.1c_{\text{mat}(0)} \\ 0.1c_{\text{mat}(0)} & c_{\text{mat}}(\bar{\epsilon}_p) < 0.1c_{\text{mat}(0)} \end{cases}, \quad (34)$$

where  $c_{\text{mat}(0)}$  is the initial cohesion of rock material;  $\bar{\epsilon}_{p(\text{crit})}$  is the critical plastic strain.

### 2.4.2 GK Damage

We use the GK damage model to describe the tensile failure of rock material (Douillet-Grellier et al. 2016a; Grady and Kipp 1980; Raymond et al. 2019). In the model, the damage state is determined based on the effective tensile strain  $\bar{\epsilon}$  and its threshold value  $\epsilon_D^0$ , which is expressed as

$$F_D(\bar{\epsilon}, \epsilon_D^0) = \bar{\epsilon} - \epsilon_D^0, \quad (35)$$

$$\bar{\epsilon} = \tilde{\sigma}_{\text{max}} / (K + \frac{4}{3}G), \quad (36)$$

$$\epsilon_D^0 = (Vk)^{-\frac{1}{m}}, \quad (37)$$

where  $\tilde{\sigma}_{\text{max}}$  is the maximum principal stress under tension;  $V$  is the volume of the material particle;  $m$  and  $k$  are the Weibull's parameters controlling the fracture activation. If  $\bar{\epsilon} > \epsilon_D^0$ , damage occurs in the rock material, which is measured by the damage parameter  $D$  varying between 0 and 1 and calculated by

$$\frac{dD^{\frac{1}{3}}}{dt} = \frac{1}{3}c_g \alpha^{\frac{1}{3}} \bar{\epsilon}^{\frac{1}{3}}, \quad (38)$$

$$\alpha = \frac{8\pi k(m+3)^2}{(m+1)(m+2)}, \quad (39)$$

where  $c_g$  is the crack growth speed during dynamic failure and usually regard as 0.4 times the speed of sound  $c_s$  in rock material. If  $D = 1$ , tensile failure occurs, resulting in a zero-stress state. Finally, the tensile component of the principal stress tensor is corrected by  $D$ , which yields

$$\tilde{\sigma}_i \leftarrow (1 - D)\tilde{\sigma}_i, \quad (40)$$

where  $\tilde{\sigma}_i$  is the principal stress under tension that is ensured by  $\tilde{\sigma}_i \in [\sigma_1, \sigma_3, \sigma_3]$ , and  $\tilde{\sigma}_i \geq 0$ . Next, the updated principal stress tensor is rotated back to the original coordinate frame to form the final total stress considering the strain damage.

## 2.5 MPM Solution

This section provides the specific implementation procedures of the MPM framework to be constructed. Recall that the motivation for this study is to numerically study the rock spalling/failure induced by a filled flaw. To this end, we implement the coupling of the DP plasticity model, the GK damage model and the PTS contact formulation within the WLS-MPM framework. We utilize the Euler explicit time integration scheme to solve the discretized governing equations in the framework. The computational cycle of the MPM is divided into the following main blocks, as summarized in Fig. 2.

1. At Eulerian grid nodes. The computational Eulerian grid and material properties are defined and the variables at Lagrangian particles such as mass, volume, position, velocity, stress, and other material internal variables are initialized before proceeding here. Next, we compute the shape functions (Eqs. 14 and 15) constructed using the WLS local approximation and their gradient, and the lumped mass matrix (Eq. 20). Information is transferred from particles to grid nodes (P2G). Then, we calculate, respectively, the nodal internal forces (Eq. 21), body forces and nodal external forces (Eq. 22). In addition, the normal and tangential contact forces after employing the PTS contact algorithm are also calculated (Eqs. 23 and 24). Finally, we solve the discretized momentum equation to obtain the nodal velocities (Eq. 18).

2. At Lagrangian particles. First, we transfer the nodal velocities from the Eulerian grid to particles (Eq. 6), and further update the positions of particles (G2P). After this, the computational grid is reset. It needs to be noticed that following the modified update stress last (MUSL) scheme (Sulsky et al. 1994) the nodal velocities are updated using the WLS global approximation (Eqs. 16 and 17). With that, the incremental strain is evaluated. Next, we perform the constitutive calculation involving DP plasticity (Eqs. 30–34) and GK damage (Eqs. 35–40). See Deb and Pramanik (2013) for more implementation details on the DP plasticity model including strain softening. From this, the total stress is updated. Finally, we enter the next time step and repeatedly execute the above computational cycle.

## 3 Simulations of Benchmark Problems

To demonstrate the effectiveness of the proposed MPM framework introduced above, we perform a set of benchmark simulations. The first is the circular opening problem commonly tested for opening-induced elastic stress and displacement redistribution in subsurfaces under high in situ stress. The benchmark is useful for validating the ground responses after the excavation of underground openings. The second is the well-known penny-shaped crack problem in the field of fracture mechanics which aims to benchmark the stress distribution near the tip of the pre-existing crack, and then the new cracks' initiation and propagation. The last one is the crack propagation problem under uniaxial compression used for demonstrating the ability to capture both shear and tensile failure and model the interplay between filler and the pre-existing crack.

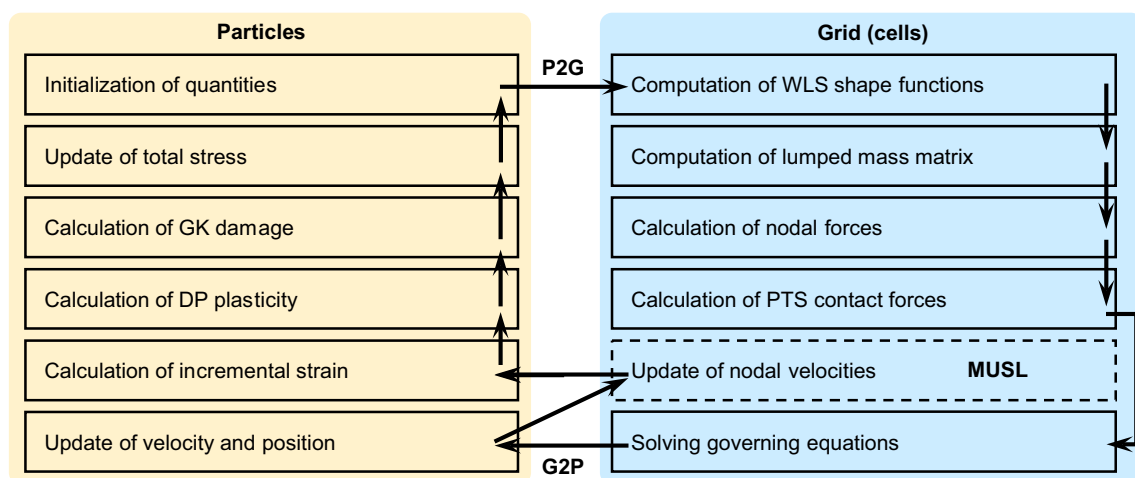


**Fig. 2** The computational flow of the coupled DP plasticity and GK damage MPM framework involving the PTS contact algorithm

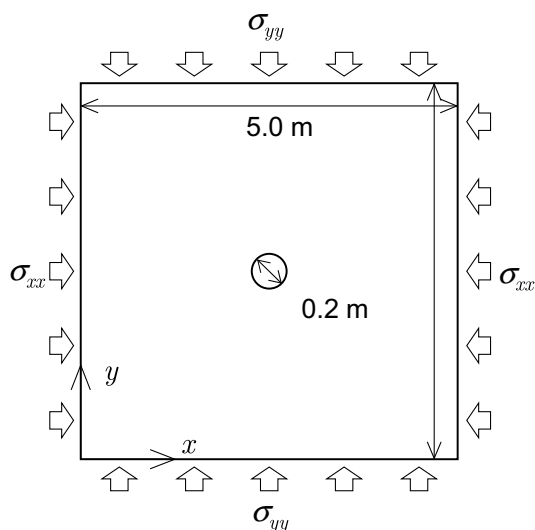


Fig. 3 Schematic of the circular opening problem

### 3.1 The Circular Opening Problem

This section compares the results of the MPM simulation by this study and the analytical solution from Howard and Fast (1970) in the case of circular opening. Figure 3 shows the geometry and boundary conditions of the circular opening problem under plane strain assumption (Nasehi and Mortazavi 2013). In this case, a circular opening with a 0.2 m diameter is cut onto a 5.0 m × 5.0 m plane strain section; the horizontal and vertical effective compressive stresses, namely  $\sigma_{xx} = 20$  MPa, and  $\sigma_{yy} = 10$  MPa, are applied to the boundary surfaces. The elastic properties of the rock material used are given as follows: Young’s modulus  $E = 22.41$  GPa, Poisson’s ratio  $\nu = 0.2313$ , and density  $\rho = 2500$  kg/m<sup>3</sup>.

For this problem, the analytical solution for the stress field with the assumption of an infinite isotropic elastic medium is given by Howard and Fast (1970):

$$\sigma_r = \frac{1}{2}(\sigma_H + \sigma_h) \left(1 - \frac{a^2}{r^2}\right) + \frac{1}{2}(\sigma_H - \sigma_h) \left(1 + 3\frac{a^4}{r^4} - 4\frac{a^2}{r^2}\right) \cos 2\theta + P\frac{a^2}{r^2}, \tag{41}$$

$$\sigma_\theta = \frac{1}{2}(\sigma_H + \sigma_h) \left(1 + \frac{a^2}{r^2}\right) - \frac{1}{2}(\sigma_H - \sigma_h) \left(1 + 3\frac{a^4}{r^4}\right) \cos 2\theta - P\frac{a^2}{r^2}, \tag{42}$$

where  $\sigma_r$  and  $\sigma_\theta$  are the radial and tangential stresses;  $\sigma_H$  and  $\sigma_h$  are the major and minor far-field principal stresses, namely  $\sigma_H = \max(\sigma_{xx}, \sigma_{yy})$ , and  $\sigma_h = \min(\sigma_{xx}, \sigma_{yy})$ ;  $\theta$  is the angle measured counter-clockwise from the  $\sigma_H$  direction;  $r$  is the distance from the center of the opening;  $a$  is the radius of the circular opening;  $P$  is the pressure acting on the opening surface and usually the injected fluid pressure and is equal to zero in this study. In addition, the MPM framework proposed by this study is used to numerically solve the circular opening problem. In the model, the grid spacing is 0.01 m, and two material particles in each coordinate direction are set per grid cell, and thus a total of 998,696 particles are created.

Figure 4 shows the stresses obtained from the analytical calculations and the MPM simulations. In addition, the elastic stress field obtained using the MPM is depicted in Fig. 5. To verify the MPM for elastic results, the horizontal ( $\sigma_{xx}$ ) and vertical ( $\sigma_{yy}$ ) stress distributions at two locations are extracted: (a)  $\sigma_{xx} = \sigma_\theta(\theta = 0^\circ)$  and  $\sigma_{yy} = \sigma_r(\theta = 0^\circ)$  along the  $x$  direction through the circular opening (Fig. 4a); (b)  $\sigma_{xx} = \sigma_r(\theta = 90^\circ)$  and  $\sigma_{yy} = \sigma_\theta(\theta = 0^\circ)$  along the  $y$  direction through the circular opening (Fig. 4b). As shown in Fig. 4, the measured results in the simulation agree well

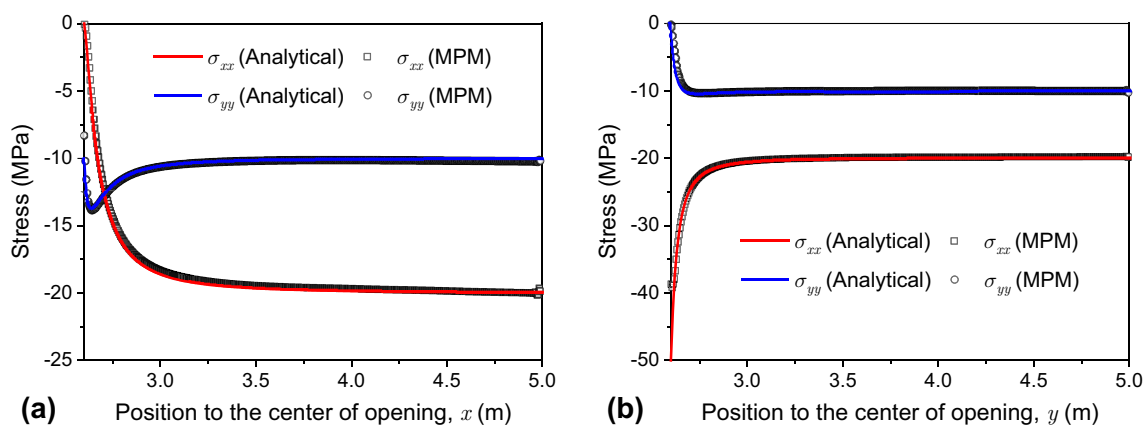
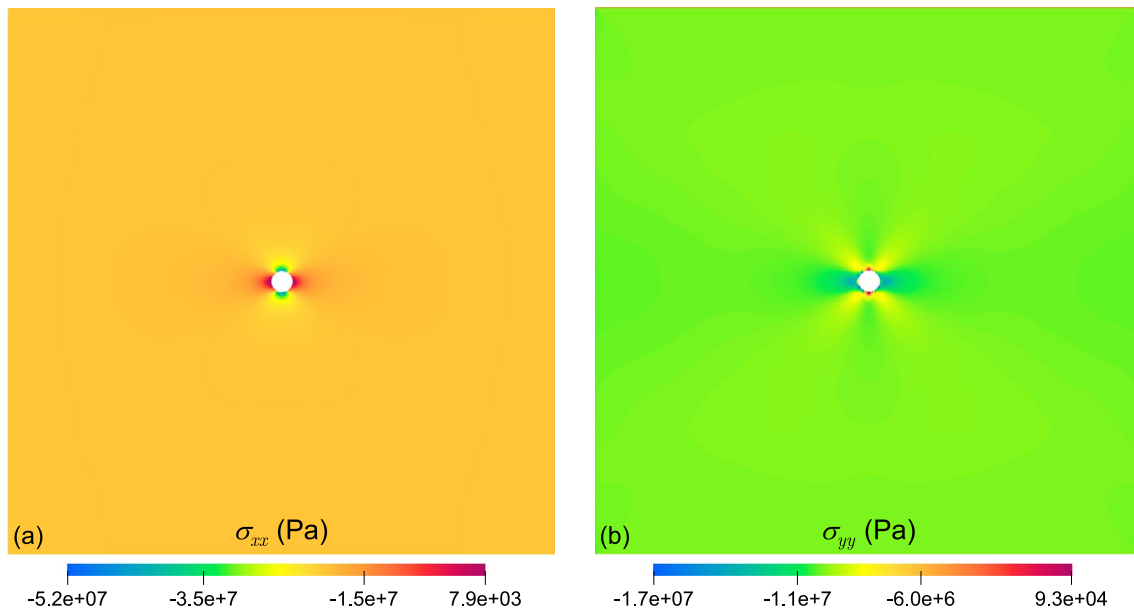
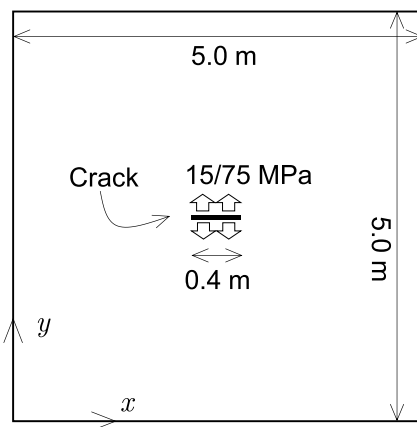


Fig. 4 Comparison between the stresses ( $\sigma_{xx}$  and  $\sigma_{yy}$ ) obtained from the MPM simulation (open shapes) and the analytical solution (solid lines) of the circular opening problem: **a** along the  $x$  direction through

the circular opening ( $y = 2.5$  m) and **b** along the  $y$  direction through the circular opening ( $x = 2.5$  m)



**Fig. 5** **a** Horizontal and **b** vertical stresses obtained from the MPM simulation of the circular opening problem



**Fig. 6** Schematic of the penny-shaped crack problem

with the analytical solutions. The only less desirable one in comparison occurs near the circular opening and the outer boundaries, primarily reflected in the radial stress. This is mainly caused by the difference between the MPM discretization of the circular opening and its exact representation in analytical calculations, which probably leads to the stress concentration. The error between the two results is expected to decrease with increasing spatial discretization resolution in the MPM, similar to that from Douillet-Grellier et al. (2016b) where the mesh-free SPH is applied.

### 3.2 The Penny-Shaped Crack Problem

The case for the validation of the constructed MPM framework in correctly predicting the tensile failure of rock material is the penny-shaped crack problem, where the particles in two layers of grid cells along the crack length are designated to be deleted as the initial crack. Figure 6 shows the geometry and loading conditions of the problem where the plane strain state is assumed. In this case, a line crack with a 0.4 m length is cut onto a 5.0 m  $\times$  5.0 m section; there are no external loads applied to the rock material but the line crack is pressurized with a constant  $P = 15$  MPa or 75 MPa. In addition to the elastic properties same as those used in the circular opening problem, the plasticity and damage properties are given here: friction angle  $\phi_{\text{mat}} = 32.5^\circ$ , dilatancy angle  $\psi_{\text{mat}} = 8.125^\circ$ , cohesion  $c_{\text{mat}(0)} = 24.8$  MPa, critical plastic strain  $\bar{\epsilon}_{p(\text{crit})} = 0.1$ , Weibull's parameters  $k = 1.1798 \times 10^{29}$  and  $m = 7.5$ . Using the MPM, two simulations are performed: one only considering the elastic behavior under loading with  $P = 15$  MPa, and the other considering the elastoplastic damage evolution during loading with  $P = 75$  MPa. The grid spacing is 0.02 m, and 249,840 particles are created. As a comparison, the analytical solution for the penny-shaped crack problem in 2D under constant pressure is given by Sneddon (1946) and Douillet-Grellier et al. (2017):

$$u_y(x, 0) = (1 - \nu^2) \frac{2P}{E} \sqrt{c^2 - x^2} \left( 1 - \sqrt{1 - \frac{a^2}{c^2}} \right), \quad (43)$$

$$\sigma_{xx}(x, 0) = \sigma_{yy}(x, 0) = P \left( \frac{x}{\sqrt{x^2 - c^2}} - 1 \right), \sigma_{xy}(x, 0) = 0, \quad (44)$$

where  $u_y$  is the vertical displacement;  $x$  is the distance from the center of the line crack;  $2a$  and  $2c$  are the pressurized length and initial geometrical length of the line crack, respectively.

To validate the linear elastic fracture behavior of our proposed MPM model, only the elastic behavior is considered in the first simulation ( $P = 15$  MPa). We extract the vertical displacement and stress distributions along the initial line crack. Figure 7 shows the comparison of these MPM results to the analytical results, and more detailed elastic responses resulting from the pressurized crack using MPM are depicted

in Fig. 8. The vertical displacement shows an elliptical shape along the line crack (Fig. 7a), which is consistent with the elliptical assumption in the analytical derivation. Generally, stress concentration occurs at the crack tip. However, an infinite value for stress is not allowed in numerical calculations. As a result, the crack-tip stress by the MPM is much smaller than that tends towards infinity by the analytical calculations, as seen in Fig. 7b. The resulting reduction in the tensile resistance of rock material at the crack tip leads to the discrepancies that  $u_y$  by the MPM is slightly greater near the crack tip and smaller at the center of crack, as seen in Fig. 7a. At present this is almost inevitable in numerical simulations and does not preclude the applicability of MPM in complex fracture modeling. Nevertheless, the MPM simulated results agree well with the analytical solution, which demonstrates

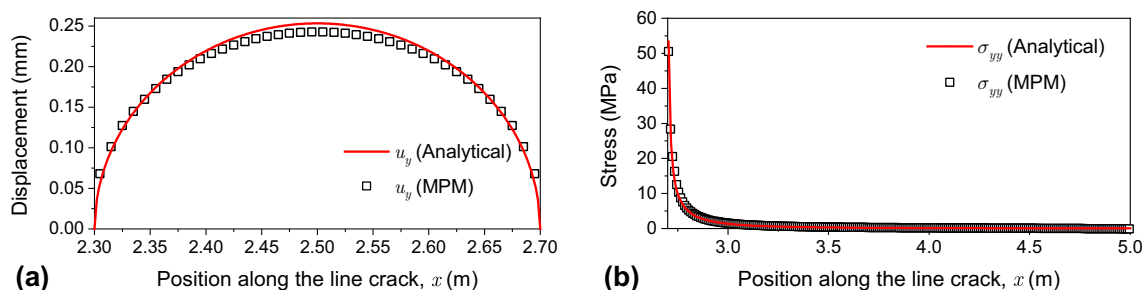


**Fig. 7** Comparison between the vertical displacements ( $u_y$ ) and stresses ( $\sigma_{yy}$ ) obtained from the MPM simulation (open squares) and the analytical solution (solid lines) for the penny-shaped crack prob-

lem: **a** along the line crack ( $x < 2.7$  m and  $y = 2.5$  m) and **b** along the  $x$  direction from the right end of line crack ( $x > 2.7$  m and  $y = 2.5$  m)

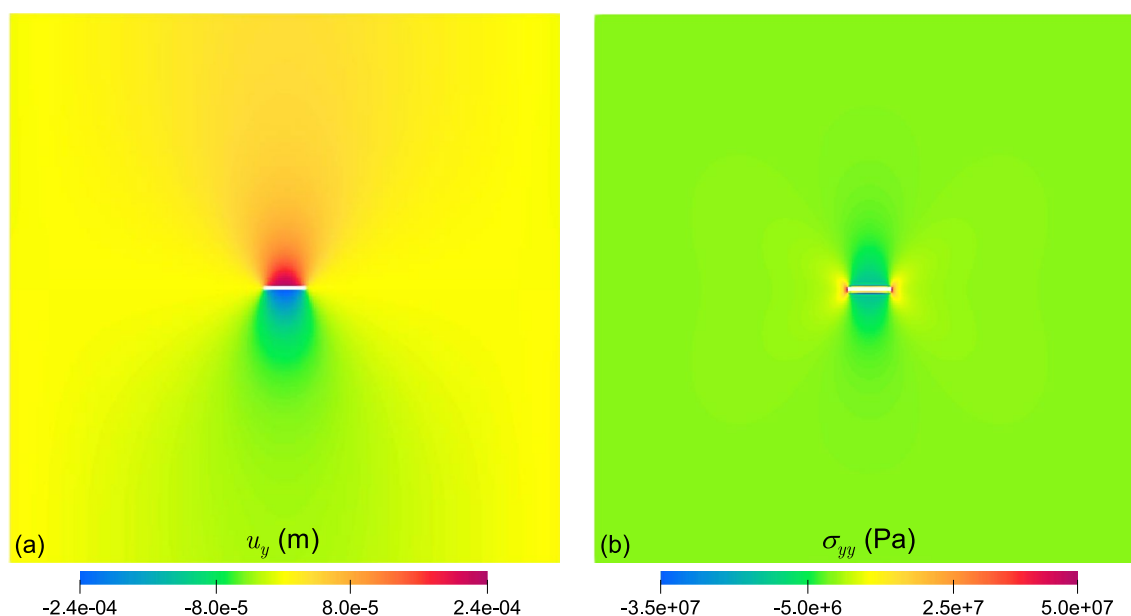


**Fig. 8** **a** Vertical displacement and **b** stress obtained from the MPM simulation of the penny-shaped crack problem only considering elastic behavior

the capability of our proposed MPM for capturing the elastic fracture behavior of the pressurized crack.

To further investigate the cracks' initiation and propagation, we consider the elastoplastic damage behavior in the second simulation ( $P = 75$  MPa). In the simulation, the load is gradually applied in the time interval from  $t = 0$  s to  $t = 0.5$  s; the parameter  $D$  reflecting tensile damage is monitored all the time ( $0 \leq D \leq 1$ ,  $D = 0$  denotes elastic or plastic undamaged, and  $D = 1$  denotes failure under tension, respectively); the number of background grid cells penetrated is used to measure the distance of crack propagation  $\Delta a$ , namely 1 cell = 0.02 m. In Fig. 9, we show the damage fields for the rock domain with a pressurized crack at  $t = 0.05$  s, 0.1 s, 0.2 s, and 0.4 s, respectively. It is observed that the new tensile cracks are initiated at the tip of the initial line crack (Fig. 9a) and then grow symmetrically outwards. The crack propagation distance  $\Delta a$  gradually increases over time

$t$  or loading pressure  $P$ , having gone from 7 to 22 cells and then 72 cells (Fig. 9b–d). The damaged but unfilled areas ( $0 < D < 1$ ) are mainly located near the tip of new cracks, which implies the subsequent tensile crack propagation. Furthermore, plasticity never happens during the whole loading process. These observations confirm that the proposed MPM framework can capture the initiation and propagation of tensile cracks, and the evolution from elasticity to damage and then failure regimes.

### 3.3 The Crack Propagation Problem

In this section, we apply the constructed MPM framework to simulate the mixed tensile-shear failure and the interplay between filler and specimen in uniaxial compression tests. First, we focus on the MPM simulation of uniaxial compression of sandstone specimens with an open flaw. The

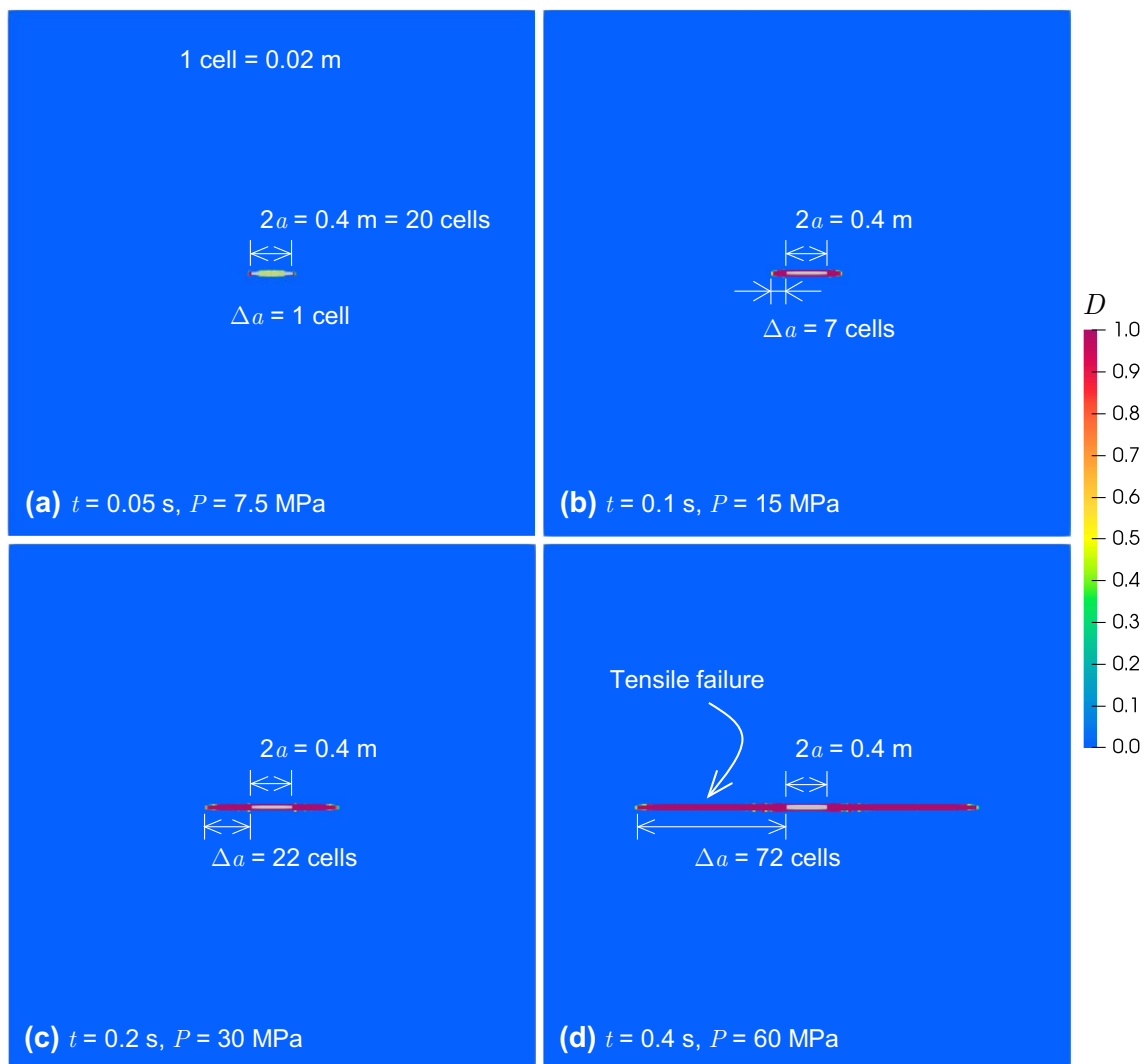
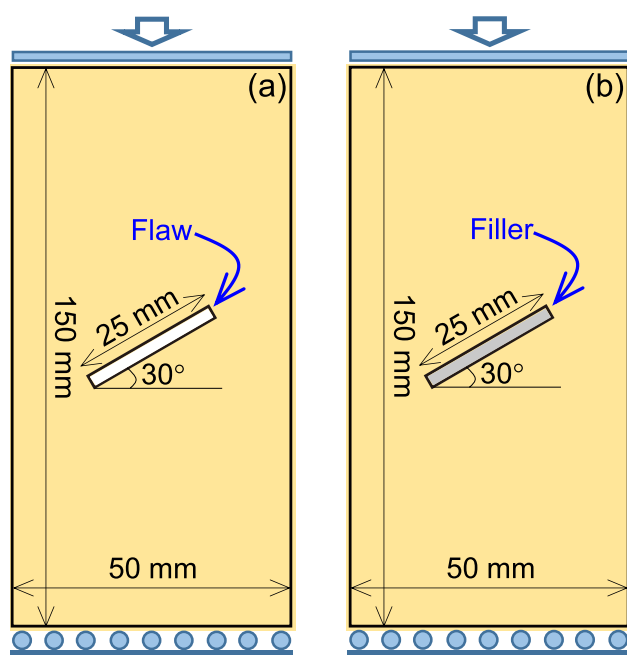


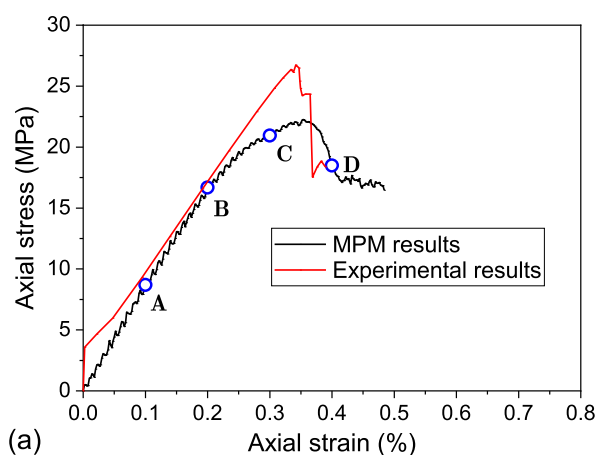
Fig. 9 Initiation and propagation of tensile cracks during continuous loading



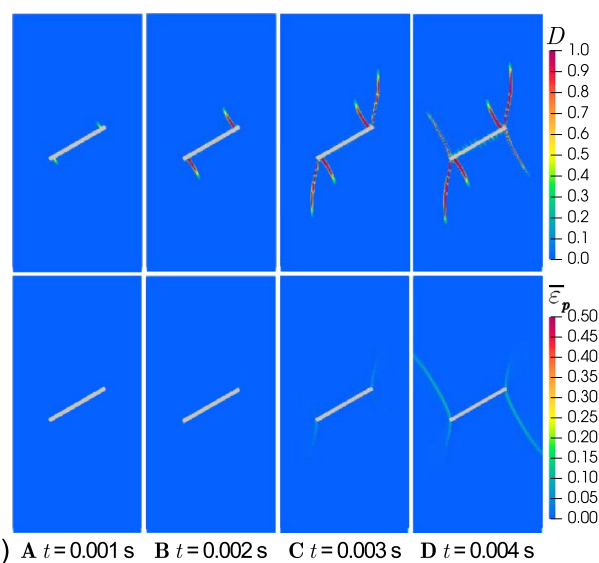
**Fig. 10** Schematic of sandstone specimens under uniaxial compression (Miao et al. 2018): **a** with an open flaw and **b** with a rigid-filled flaw

schematic of the uniaxial compression test conducted by Miao et al. (2018) is shown in Fig. 10a. In the test, a 50 mm × 150 mm sandstone specimen with an open flaw is prepared; the open flaw is 25 mm in length and 2 mm in width, and has a 30° inclination angle to the horizontal direction; free-slip boundary conditions are imposed at the top and bottom of the specimen; the sample is loaded under a constant velocity of 0.1 m/s with a rigid upper platen. The common material properties used here follow the ones given by Miao et al. (2018): Young's modulus  $E=9.87$  GPa, Poisson's ratio  $\nu=0.22$ , density  $\rho=2520$  kg/m<sup>3</sup>, friction angle  $\phi_{\text{mat}}=38^\circ$ , dilatancy angle  $\psi_{\text{mat}}=9.5^\circ$ , and  $c_{\text{mat}(0)}=13.0$  MPa. The damage-related parameters are obtained from Raymond et al. (2019): critical plastic strain  $\bar{\epsilon}_{p(\text{crit})}=0.1$ , Weibull's parameters  $k=7.0 \times 10^{35}$ , and  $m=9.0$ . Note that the background grid must be fine enough to generate the real geometry for the flaw explicitly. In this study, the width of the flaw always has to be more than twice the grid spacing. In the MPM model, the grid spacing is 0.5 mm, and 79,294 particles are created.

Figure 11a compares the uniaxial compression stress–strain curves obtained from the MPM simulation and the experimental results by Miao et al. (2018). The mechanical responses exhibited by the MPM model and the experiment are very similar qualitatively but when near the peak failure, the axial stress values are different. Compared to the experiment, the MPM simulation leads to smaller peak stress. This difference arises due to the upper free-slip



(a)



(b) A  $t=0.001$  s B  $t=0.002$  s C  $t=0.003$  s D  $t=0.004$  s

**Fig. 11** Crack evolution for the sandstone specimen with an open flaw under uniaxial compression: **a** comparison between the axial stress–strain curves obtained from the MPM simulation and the experimental results (Miao et al. 2018); **b** evolution of damage ( $D$ ) and accumulated plastic strain ( $\bar{\epsilon}_p$ )

boundary being impossible to achieve in the physical experiment. More horizontal displacement is observed in the post-failure MPM specimen. Moreover, plastic softening occurs before the peak stress is reached during the MPM simulation. Figure 11b shows the evolution of accumulated plastic strain  $\bar{\epsilon}_p$  and damage  $D$  with loading time. The tensile failure first initiates at the tip of the pre-existing flaw and grows up to the wing cracks. With the continuous loading, the tensile and shear horsetail cracks, and the tensile anti-wing and oblique secondary cracks appear successively until the sample is penetrated by the cracks, as shown in Fig. 12a, b. The dominant crack propagation paths are partially consistent with the experimental results shown in Fig. 12c. The crack types are summarized in Fig. 12d, which are the same as Park and Bobet (2009) and Pan et al. (2020a). This confirms

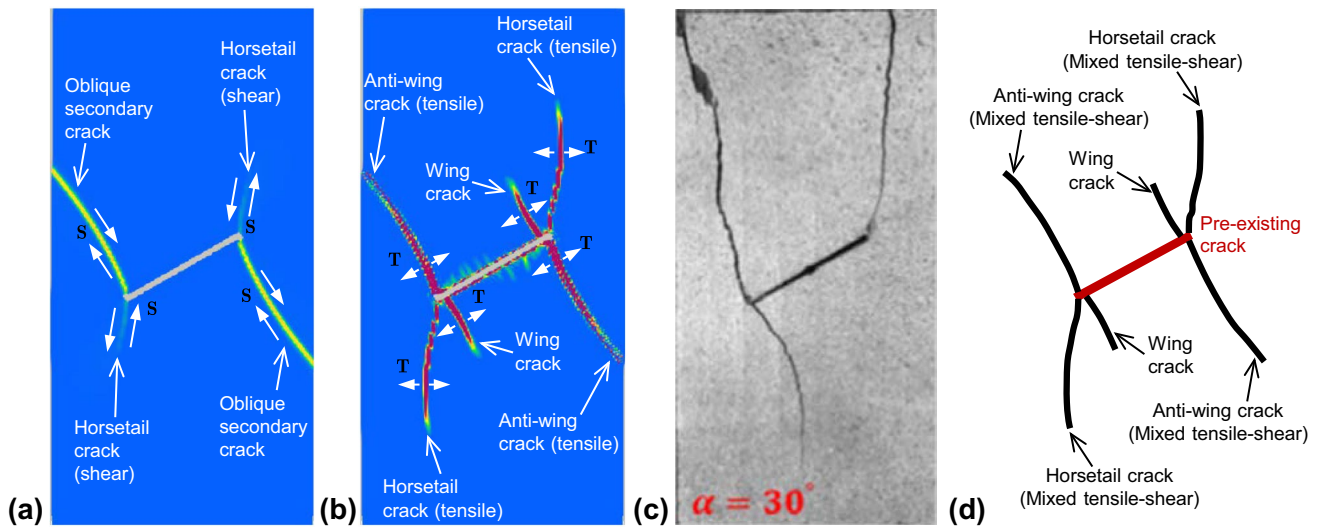


**Fig. 12** Crack types for the sandstone specimen with an open flaw under uniaxial compression: **a** shear cracks; **b** tensile cracks; **c** experimental results by Miao et al. (2018); **d** crack types observed in the MPM simulation by this study

that the MPM can capture the mixed tensile-shear fracture behavior correctly.

Second, we systematically investigate how the different contact frictions between filler and sandstone may influence the crack behavior of sandstone specimen with a rigid-filled flaw under uniaxial compression (Fig. 10b). Figure 13 shows the uniaxial compression stress–strain curves under different contact friction coefficient  $\mu_{con}$  and cohesion  $c_{con}$ . In the process of uniaxial compression, the sandstone around the pre-existing flaw is gradually in contact with the rigid filler, and a frictional contact is motivated to hinder the sequential deformation. This is confirmed by inspection of the distributions of  $\tilde{\sigma}_{max}$  around the pre-existing flaw. From Fig. 14a, the area near the open

flaw is under tension and tends to have tensile failure due to its extremely high  $\tilde{\sigma}_{max}$ . Instead, the area near the rigid-filled flaw is under compression, as shown in Fig. 14b. In general, greater  $\tilde{\sigma}_{max}$  mainly distributes at the tip of new cracks. The contact interaction between the filler and sandstone after the filling plays a dominant role in the increase of peak stress. In addition, the failure patterns changes due to the filling that the coplanar secondary and tertiary tensile cracks newly appear, as shown in Fig. 14c, d.

In addition to the normal contact support from the rigid filler, the tangential contact force also has a positive effect due to the 30° inclination angle. As shown in Fig. 13, the increase of  $\mu_{con}$  between the filler and sandstone enhances the peak stress but that is not the case regarding  $c_{con}$ . With

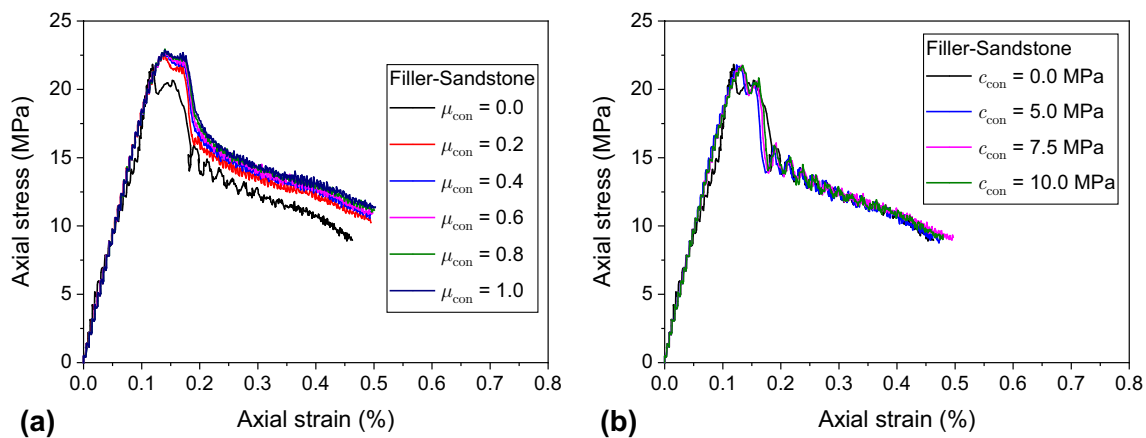


**Fig. 13** Axial stress–strain curves for the rigid-filled sandstone specimens with **a** different contact friction coefficients and **b** cohesion under uniaxial compression

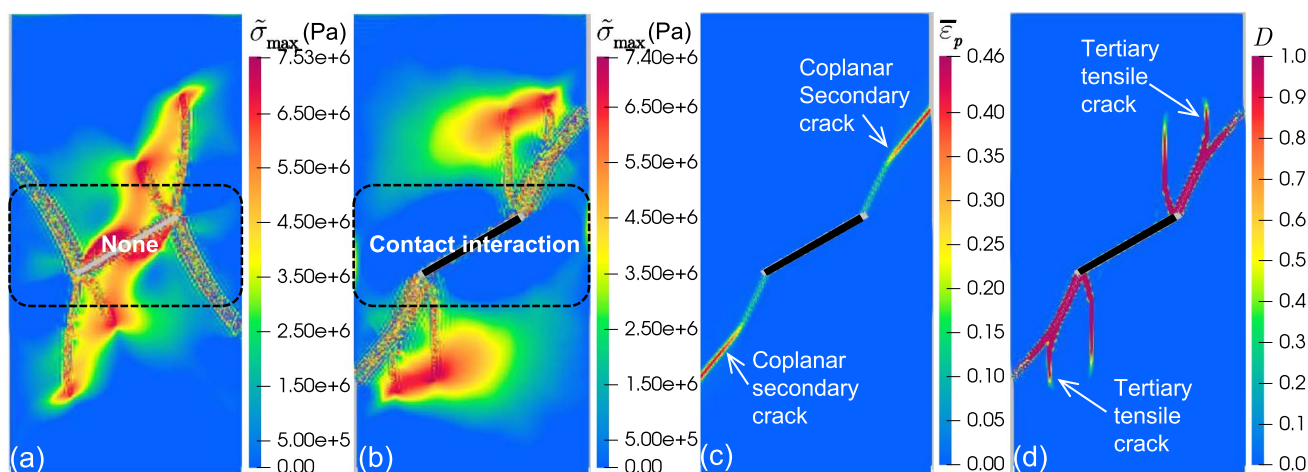


**Fig. 14** The maximum principal stress under tension is extracted for comparison: **a** sandstone specimen with an open flaw; **b** sandstone specimen with a rigid-filled flaw. Post-failure results ( $t=0.006$  s) for

the rigid-filled sandstone specimen ( $\mu_{\text{con}}=0.6$ ,  $c_{\text{con}}=0$  MPa) under uniaxial compression: **c** shear cracks; **d** tensile cracks

the increase of  $c_{\text{con}}$ , the axial strain at peak failure slightly increases. For the cases considering  $\mu_{\text{con}}$ , we set  $c_{\text{con}}=0$ , resulting in  $f_i^{\text{tan}(\text{max})} = \mu_{\text{con}} \|\mathbf{f}_i^{\text{nor}}\|$ . When  $\mu_{\text{con}}$  is relatively small ( $\|\mathbf{f}_i^{\text{stick}}\| \geq f_i^{\text{tan}(\text{max})}$ ), slip contact occurs and then the tangential contact force is influenced by the variation of  $\mu_{\text{con}}$ . Similarly, for the cases considering  $c_{\text{con}}$ , we set  $\mu_{\text{con}}=0$ , resulting in  $f_i^{\text{tan}(\text{max})} = A_{\text{con}} c_{\text{con}}$ . When  $\|\mathbf{f}_i^{\text{stick}}\| < f_i^{\text{tan}(\text{max})}$ , stick contact occurs and the tangential contact force only depends on  $\mathbf{f}_i^{\text{stick}}$ . From Fig. 13b, the stick contact state always remains when  $c_{\text{con}} > 5.0$  MPa. Overall, the improvement of tangential frictional contact on the stability of the flawed specimen is not as great as expected. This may be due to the fact that the contact surfaces between the filler and sandstone after the filling are not precisely modeled in the MPM simulations, which is reflected in the scattered stress concentrations around the rigid filler shown in Fig. 15. It is worth noting that the discretization method commonly used in mesh-free methods is adopted where the geometry of contact interface is modeled by the particles in the regular grid cell, which usually results in rough surfaces for irregularly placed structures.

#### 4 Simulations of Rock Spalling/Failure

On top of the benchmarks conducted above, in this section, we continue to investigate the mechanism of rock spalling/failure around an underground opening under different geological conditions, with the purpose of thoroughly testing the applicability and effectiveness of our proposed MPM framework. Three tunnel opening models are considered:

(a) without flaw, (b) with a nearby open flaw, and (c) with a nearby rigid-filled flaw. We use the constructed MPM framework to simulate the whole failure process of those models under plane strain compression. A series of plane strain compression tests were conducted by Pan et al. (2020b) on the spalling process of the tunnel. The schematic of the arch-shaped tunnels considered is shown in Fig. 16. Following Pan's experiments, an arch-shaped tunnel made up of 40 mm  $\times$  25 mm rectangle and 20 mm radius semicircular areas are cut within a 150 mm  $\times$  150 mm sandstone specimen (Fig. 16a); a 60 mm  $\times$  2 mm open flaw adjacent to the tunnel is first cut (Fig. 16b) and then filled with rigid material (Fig. 16c); free-slip boundary conditions are imposed at the four sides of the specimen; a rigid upper platen is used to load the samples in a constant downward velocity of 0.1 m/s at the top. Similarly, the damage parameters from Raymond et al. (2019) are still used here, and the material properties are provided by Pan et al. (2020b) as follows: Young's modulus  $E=18.4$  GPa, Poisson's ratio  $\nu=0.12$ , density  $\rho=2364$  kg/m<sup>3</sup>, friction angle  $\phi_{\text{mat}}=39^\circ$ , dilatancy angle  $\psi_{\text{mat}}=9.75^\circ$ , and  $c_{\text{mat}(0)}=25.0$  MPa. The spacing of the background grid is 1.0 mm, and the specimens without flaw and with an open flaw are modeled using 83,430 and 83,003 particles, respectively.

The axial stress–displacement curves for the tunnels under the three geological conditions are shown in Fig. 17. Qualitatively, the axial stress increases with increasing axial displacement and its increase tends to ease up at the later loading stage; the peak stress does not appear; the axial stress decreases at a certain level due to the nearby open flaw but increases due to the filling of open flaw. These are similar to that revealed by the experiments in Pan et al.

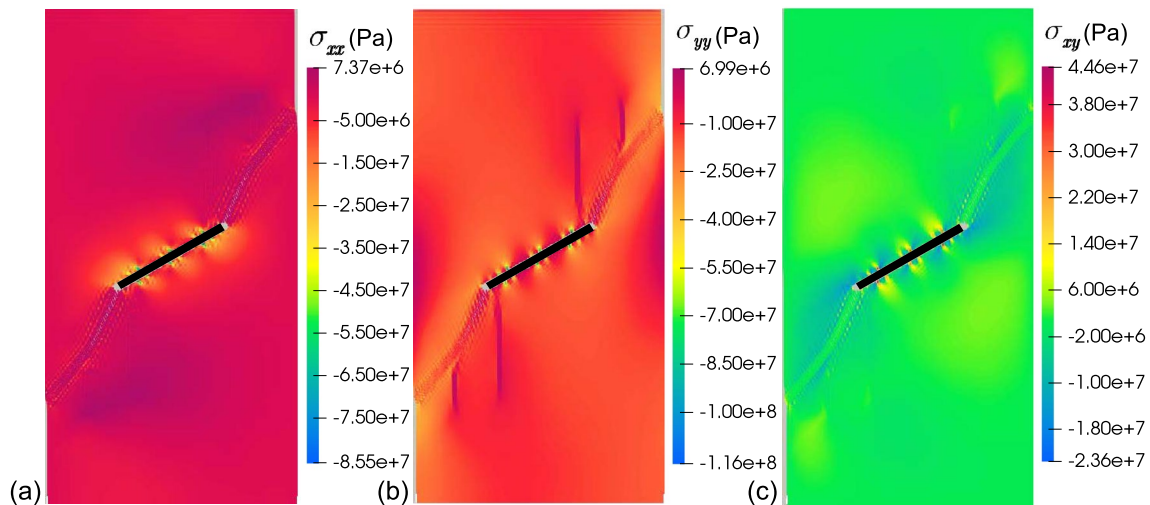


**Fig. 15** Stresses ( $t=0.006$  s) for the rigid-filled sandstone specimen ( $\mu_{con}=0.6$ ,  $c_{con}=0$  MPa) under uniaxial compression

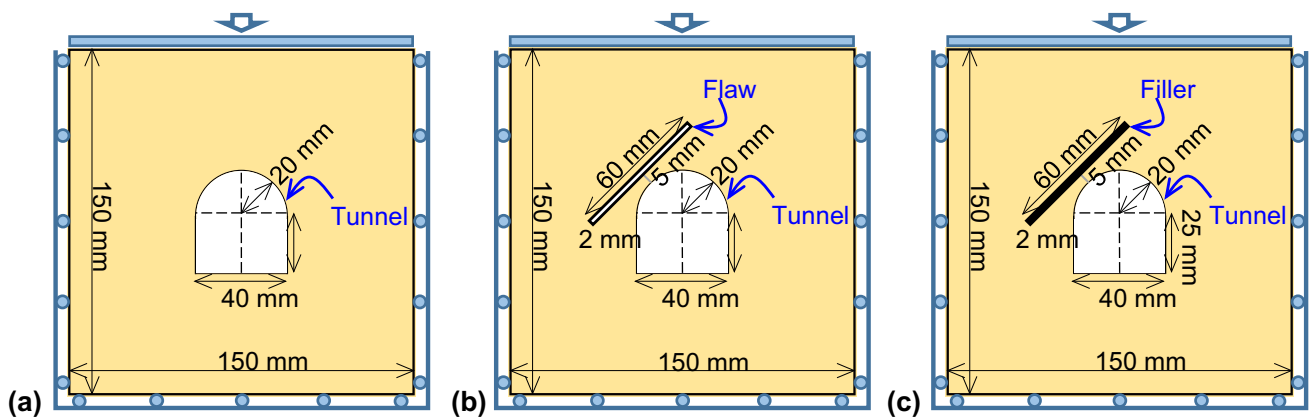


**Fig. 16** Schematic of the arch-shaped tunnels under axial displacement loading (Pan et al. 2020b): **a** without flaw, **b** with a nearby open flaw, and **c** with a nearby rigid-filled flaw

(2020b). At the initial loading stage, the axial stress significantly increases with axial displacement for the case with a rigid-filled flaw. It can be attributed that the stress concentration occurring at the two ends of the rigid filler is rapidly initiated, which reduces the stress transmission path from the upper platen to the bottom platform. Figure 18 shows the evolution of accumulated plastic strain with loading time and the post-failure results for the model without flaw. First, the symmetric distributed tensile cracks appear at the bottom of the tunnel prior to the initiation of mixed shear-tensile cracks around the two sides of the tunnel, as shown in Fig. 18d. This can serve as a contribution to recognizing the in situ stress state of the tunnel.

Second, the plastic strain is symmetrically distributed at  $t=0.008$  s and the two plastic areas are in triangular shapes (Fig. 18a). The plastic shear bands with an inclination angle of about  $55^\circ$  are localized at  $t=0.012$  s and shifted upwards (Fig. 18b), which are also accompanied by tensile failures (Fig. 18d). This lead to smaller plastic-wrapped areas, which could cause the tunnel spalling/failure. With continuous loading, new shear cracks appear at  $t=0.02$  s. The sequential appearance of multiple cracks initiated from the opening surface is the spalling process. Third, the distributions of maximum principal stress under tension and displacement in the  $x$  and  $y$  directions also can reflect the spalling area of the tunnel (Fig. 18e–g). The distinguishable responses are mainly distributed near the opening surface, specifically at

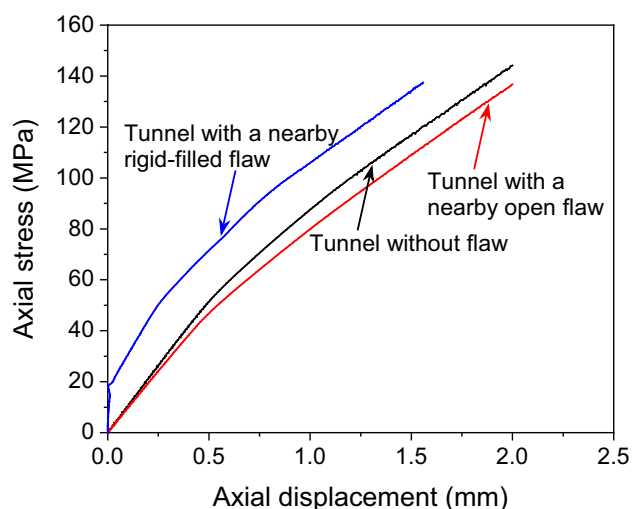


**Fig. 17** Axial stress–strain curves for the tunnels under different geological conditions

the tunnel waist. The corresponding experimental results in Pan et al. (2020b) are also presented in Fig. 18h for comparison, and the similarity between our MPM results and those in Pan et al. (2020b) demonstrates the effectiveness of the MPM simulation for rock spalling/failure simulation.

To analyze the influence of the open flaw and the rigid-filled flaw on rock spalling/failure, we present in Fig. 19 the post-failure results for the two models under plane strain compression. The spatial distributions of shear and tensile cracks change greatly due to the nearby flaw, which is obviously no longer symmetric. The open flaw hinders the transferring of loads from the top to the area at the tunnel

left waist, however, which results in the stress concentration occurring at the flaw toe and then the anti-wing shear crack (Fig. 19a). This is consistent with the experimental results in Pan et al. (2020b) presented in Fig. 19d. In addition, this spalling area can be observed by the displacement field in the  $x$  direction shown in Fig. 19c. In Pan's experiments, the stress concentration induced by an open flaw is somewhat alleviated with different filling materials. However, for the case with a rigid-filled flaw simulated in this study, the spalling at the tunnel left spandrel is exacerbated and the new mixed shear-tensile crack connected from the flaw toe to the tunnel corner is triggered, as shown in Fig. 19e, f.

The difference between the two arises from the rigid filler serving as a load transfer medium by means of contact with the surrounding sandstone. Meanwhile, the filling with rigid materials introduces extreme material heterogeneity, which could lead to a more serious stress concentration and even severe failure such as the newly connected crack. These causes could occur in the grouting process for the filling of pre-existing open flaws. Thus, grouting is applied to fill the nearby open flaw for tunnel stability while simultaneously concerning the grouting pressure and the mechanical properties of filling material. In addition, when the spalling and band failure at the tunnel left spandrel and corner propagate towards the rigid-filled flaw until the failure area is simultaneously connected, the massive collapse occurs at the tunnel left waist, as shown in Fig. 19g. The spalling profiles occurred at the tunnel right waist and the tunnel left corner are also revealed in the experiment (Fig. 19h). All these observations suggest that the proposed MPM framework is appropriate and applicable to rock spalling/failure simulations induced by a filled flaw.

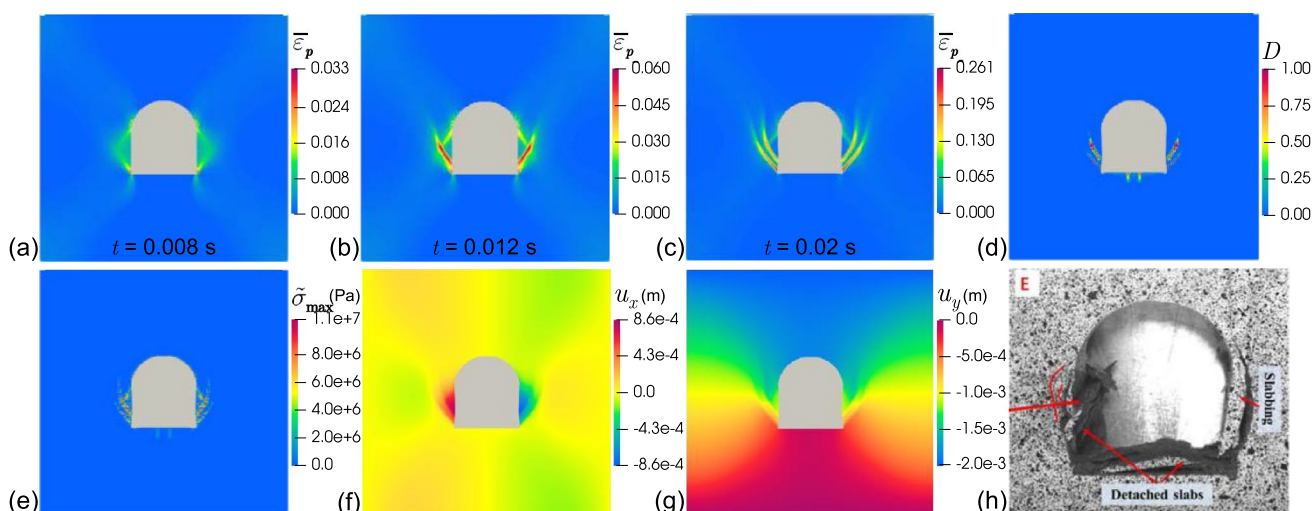


**Fig. 18** Spalling evolution and post-failure results for the tunnel without flaw: **a–c** accumulated plastic strain at  $t=0.008$  s,  $0.012$  s and  $0.02$  s, respectively; **d** damage; **e** maximum principal stress under

tension; **f, g** displacement in the  $x$  and  $y$  directions, respectively; **h** experimental results by Pan et al. (2020b)

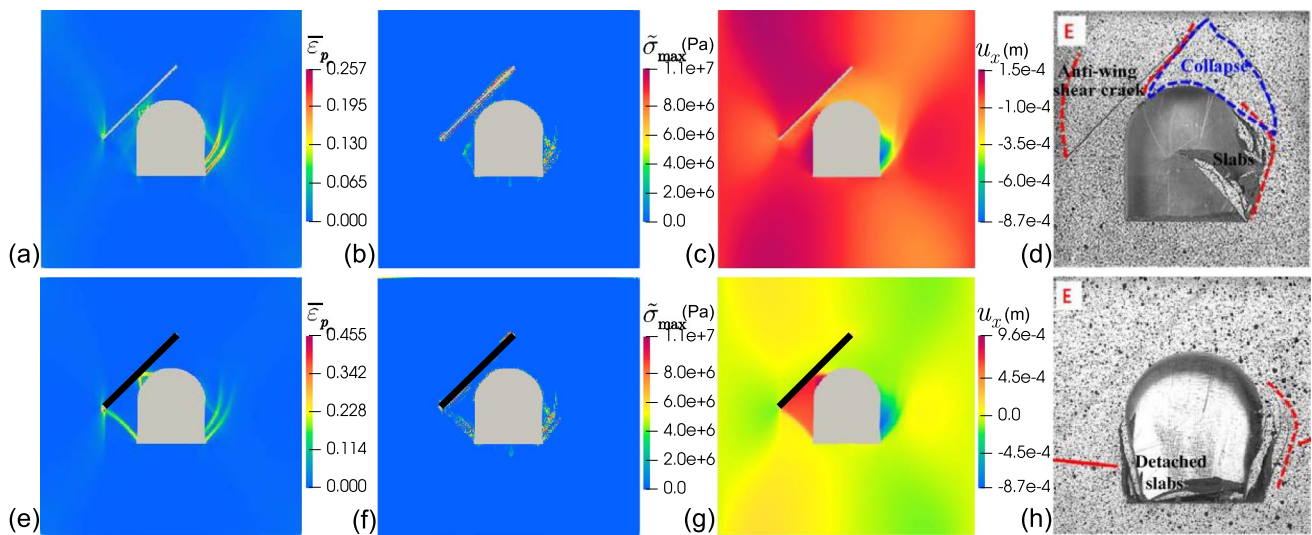


**Fig. 19** Post-failure results for the tunnels with a nearby open flaw (top panels) and a rigid-filled flaw (bottom panels): **a, e** accumulated plastic strain; **b, f** maximum principal stress; **d, g** displacement in the  $x$  direction; **d, h** experimental results by Pan et al. (2020b)

## 5 Conclusions

In the present paper, we have successfully constructed a WLS-MPM framework for the simulation of rock spalling/failure induced by a filled flaw. In the framework, the coupled DP plasticity and GK damage model is used to capture the mixed tensile-shear failure in the spalling/failure of underground openings, and the PTS contact formulation is employed to model the contact interaction between pre-existing filled flaws and surrounding rock. We benchmark the framework on a series of classical problems. The elastic stress response by the MPM framework agrees well with analytical solutions for the circular opening problem. For the penny-shaped crack problem, compared to analytical solutions and experimental observations, the elastic fracture behavior, the initiation and propagation of the tensile crack, and the evolution from elasticity to damage are accurately captured by the MPM framework. The MPM simulations and experimental results are compared with uniaxial compression tests, which confirms that the MPM framework can simulate the mixed tensile-shear failure and the interplay between rigid filler and surrounding materials correctly.

We have also performed simulations of plane strain compression tests for arch-shaped tunnel openings under different geological conditions to investigate the influence of rigid-filled flaws on rock spalling/failure. Using the proposed MPM framework, the spalling process is numerically reproduced by the sequential appearance of multiple cracks initiated from the opening surface. The open flaw results in the stress concentration at the flaw toe and subsequently

the anti-wing shear crack, which was also observed by Pan et al. (2020b). Due to the filling of the nearby open flaw, the spalling at the tunnel left spandrel is exacerbated and the new mixed shear-tensile crack connected from the flaw toe to the tunnel corner is induced. When the area formed by the spalling and band failure at the tunnel left spandrel and corner is connected to the filler, a massive collapse could occur at the tunnel left waist.

In addition, we notice that the deformation of filler and grouting pressure into the open flaw are other key factors influencing the spalling/failure of underground openings, which are not considered in this study. Nevertheless, the presented MPM framework generalizes the coupled plasticity-damage large deformation mechanics for diverse fracture processes such as tensile, shear and mixed failure, which has been extended to resolve filler-induced spalling phenomena by introducing PTS contact algorithm in this study and further deformable contact formulation in future works. Similarly, the framework can be easily adjusted to incorporate other rock fracturing related simulations, such as hydraulic fracturing by appropriate treatment of strong discontinuity and fluid flow in fractured rocks. Our results provide a convenient framework for multiphysics fracture modeling, with potential applications in areas such as fracture propagation simulations during grouting in nearby open flaws for underground opening stability.

**Acknowledgements** This work is supported by the China Postdoctoral Science Foundation (2022M711494), the Shenzhen Science and Technology Program (JCYJ20220530113612028) and the Guangdong Provincial Key Laboratory of Geophysical High-resolution Imaging Technology (2022B1212010002).

**Data availability** The datasets generated during and/or analyzed during the current study are available from the authors on reasonable request.

## Declarations

**Conflict of interest** The authors declare that they have no conflict of interest.

## References

- Bandara S, Soga K (2015) Coupling of soil deformation and pore fluid flow using material point method. *Comput Geotech* 63:199–214
- Bardenhagen SG, Kober EM (2004) The generalized interpolation material point method. *Comput Model Eng Sci* 5(6):477–496
- Burghardt J, Brannon R, Guilkey J (2012) A nonlocal plasticity formulation for the material point method. *Comput Methods Appl Mech Eng* 225:55–64
- de Souza Neto EA, Peric D, Owen DR (2011) *Computational methods for plasticity: theory and applications*. Wiley, New York
- Deb D, Pramanik R (2013) Failure process of brittle rock using smoothed particle hydrodynamics. *J Eng Mech* 139(11):1551–1565
- Douillet-Grellier T, Jones BD, Pramanik R, Pan K, Albaiz A, Williams JR (2016a) Mixed-mode fracture modeling with smoothed particle hydrodynamics. *Comput Geotech* 79:73–85
- Douillet-Grellier T, Pramanik R, Pan K, Albaiz A, Jones BD, Pourpak H, Williams JR (2016b) Mesh-free numerical simulation of pressure-driven fractures in brittle rocks. In: SPE hydraulic fracturing technology conference. OnePetro
- Douillet-Grellier T, Pramanik R, Pan K, Albaiz A, Jones BD, Williams JR (2017) Development of stress boundary conditions in smoothed particle hydrodynamics (SPH) for the modeling of solids deformation. *Comput Part Mech* 4(4):451–471
- Fakhimi A, Carvalho F, Ishida T, Labuz J (2002) Simulation of failure around a circular opening in rock. *Int J Rock Mech Min Sci* 39(4):507–515
- Gong F-q, Luo Y, Li X-b, Si X-f, Tao M (2018) Experimental simulation investigation on rockburst induced by spalling failure in deep circular tunnels. *Tunn Undergr Space Technol* 81:413–427
- Grady DE, Kipp ME (1980) Continuum modelling of explosive fracture in oil shale. *Int J Rock Mech Min Sci Geomech Abstr* 3:147–157
- Hinton E, Rock T, Zienkiewicz O (1976) A note on mass lumping and related processes in the finite element method. *Earthq Eng Struct Dyn* 4(3):245–249
- Howard GC, Fast CR (1970) *Hydraulic fracturing*. New York, Society of Petroleum Engineers of AIME, 1970
- Hu Y, Fang Y, Ge Z, Qu Z, Zhu Y, Pradhana A, Jiang C (2018) A moving least squares material point method with displacement discontinuity and two-way rigid body coupling. *ACM Trans Graphics (TOG)* 37(4):1–14
- Hu Z, Liu Y, Zhang H, Zheng Y, Ye H (2021) Implicit material point method with convected particle domain interpolation for consolidation and dynamic analysis of saturated porous media with massive deformation. *Int J Appl Mech* 13(02):2150023
- Hu Z, Zhang H, Zheng Y, Ye H (2022) Phase-field implicit material point method with the convected particle domain interpolation for brittle–ductile failure transition in geomaterials involving finite deformation. *Comput Methods Appl Mech Eng* 390:114420
- Huang F, Zhu H, Xu Q, Cai Y, Zhuang X (2013) The effect of weak interlayer on the failure pattern of rock mass around tunnel—scaled model tests and numerical analysis. *Tunn Undergr Space Technol* 35:207–218
- Jacobsson L, Appelquist K, Lindkvist JE (2015) Spalling experiments on large hard rock specimens. *Rock Mech Rock Eng* 48(4):1485–1503
- Jeon S, Kim J, Seo Y, Hong C (2004) Effect of a fault and weak plane on the stability of a tunnel in rock—a scaled model test and numerical analysis. *Int J Rock Mech Min Sci* 41:658–663
- Jiao Y-Y, Zhang X-L, Zhao J (2012) Two-dimensional DDA contact constitutive model for simulating rock fragmentation. *J Eng Mech* 138(2):199–209
- Kao C-S, Tarokh A, Biolzi L, Labuz JF (2016) Inelastic strain and damage in surface instability tests. *Rock Mech Rock Eng* 49(2):401–415
- Klár G, Gast T, Pradhana A, Fu C, Schroeder C, Jiang C, Teran J (2016) Drucker-Prager elastoplasticity for sand animation. *ACM Trans Graphics* 35(4):1–12
- Lee IM, Kim DH (2003) A simulation using a hybrid method for predicting fault zones ahead of a tunnel face. *Int J Numer Anal Meth Geomech* 27(2):147–158
- Li S, Liu WK (2007) *Meshfree particle methods*. Springer, New York
- Li X, Li X-F, Zhang Q-B, Zhao J (2018) A numerical study of spalling and related rockburst under dynamic disturbance using a particle-based numerical manifold method (PNMM). *Tunn Undergr Space Technol* 81:438–449
- Lisjak A (2013) Investigating the Influence of Mechanical anisotropy on the Fracturing Behaviour of Brittle Clay Shales with Application to Deep Geological Repositories. PhD, University of Toronto
- Liu Y, Ye H, Zhang H, Zheng Y (2020) Coupling lattice Boltzmann and material point method for fluid-solid interaction problems involving massive deformation. *Int J Numer Methods Eng* 121(24):5546–5567
- Mazaira A, Konicek P (2015) Intense rockburst impacts in deep underground construction and their prevention. *Can Geotech J* 52(10):1426–1439
- Miao S, Pan P-Z, Wu Z, Li S, Zhao S (2018) Fracture analysis of sandstone with a single filled flaw under uniaxial compression. *Eng Fract Mech* 204:319–343
- Nairn JA (2018) Direct comparison of anisotropic damage mechanics to fracture mechanics of explicit cracks. *Eng Fract Mech* 203:197–207
- Nakamura K, Matsumura S, Mizutani T (2021) Particle-to-surface frictional contact algorithm for material point method using weighted least squares. *Comput Geotech* 134:104069
- Nasehi MJ, Mortazavi A (2013) Effects of in-situ stress regime and intact rock strength parameters on the hydraulic fracturing. *J Petrol Sci Eng* 108:211–221
- Pan P-Z, Miao S, Jiang Q, Wu Z, Shao C (2020a) The influence of infilling conditions on flaw surface relative displacement induced cracking behavior in hard rock. *Rock Mech Rock Eng* 53(10):4449–4470
- Pan P-Z, Miao S, Wu Z, Feng X-T, Shao C (2020b) Laboratory observation of spalling process induced by tangential stress concentration in hard rock tunnel. *Int J Geomech* 20(3):04020011
- Papamichos E, Labuz J, Vardoulakis I (1994) A surface instability detection apparatus. *Rock Mech Rock Eng* 27(1):37–56
- Park CH, Bobet A (2009) Crack coalescence in specimens with open and closed flaws: a comparison. *Int J Rock Mech Min Sci* 46(5):819–829
- Raymond SJ, Jones BD, Williams JR (2019) Modeling damage and plasticity in aggregates with the material point method (MPM). *Comput Part Mech* 6(3):371–382
- Raymond SJ, Jones BD, Williams JR (2021) Fracture shearing of polycrystalline material simulations using the material point method. *Comput Part Mech* 8(2):259–272
- Sagong M, Park D, Yoo J, Lee JS (2011) Experimental and numerical analyses of an opening in a jointed rock mass under biaxial compression. *Int J Rock Mech Min Sci* 48(7):1055–1067

- Shepard D (1968) A two-dimensional interpolation function for irregularly-spaced data. In: Proceedings of the 1968 23rd ACM national conference, pp 517–524
- Shou K-J (2000) A three-dimensional hybrid boundary element method for non-linear analysis of a weak plane near an underground excavation. *Tunn Undergr Space Technol* 15(2):215–226
- Sneddon IN (1946) The distribution of stress in the neighbourhood of a crack in an elastic solid. *Proc R Soc Lond A* 187(1009):229–260
- Song L, Jiang Q, Shi Y-E, Feng X-T, Li Y, Su F, Liu C (2018) Feasibility investigation of 3D printing technology for geotechnical physical models: study of tunnels. *Rock Mech Rock Eng* 51(8):2617–2637
- Sulsky D, Chen Z, Schreyer HL (1994) A particle method for history-dependent materials. *Comput Methods Appl Mech Eng* 118(1–2):179–196
- Sulsky D, Zhou S-J, Schreyer HL (1995) Application of a particle-in-cell method to solid mechanics. *Comput Phys Commun* 87(1–2):236–252
- Tarokh A, Kao C-S, Fakhimi A, Labuz JF (2016a) Insights on surface spalling of rock. *Comput Part Mech* 3(3):391–405
- Tarokh A, Kao C-S, Fakhimi A, Labuz JF (2016b) Spalling and brittleness in surface instability failure of rock. *Geotechnique* 66(2):161–166
- Vardoulakis I, Papanastasiou PC (1988) Bifurcation analysis of deep boreholes: I. Surface instabilities. *Int J Numer Anal Methods Geomech* 12(4):379–399
- Wang J, Chan D (2014) Frictional contact algorithms in SPH for the simulation of soil–structure interaction. *Int J Numer Anal Meth Geomech* 38(7):747–770
- Wu Z, Jiang Y, Liu Q, Ma H (2018) Investigation of the excavation damaged zone around deep TBM tunnel using a Voronoi-element based explicit numerical manifold method. *Int J Rock Mech Min Sci* 112:158–170
- Yang Y, Tang X, Zheng H, Liu Q, He L (2016) Three-dimensional fracture propagation with numerical manifold method. *Eng Anal Bound Elem* 72:65–77
- York AR, Sulsky D, Schreyer HL (2000) Fluid–membrane interaction based on the material point method. *Int J Numer Methods Eng* 48(6):901–924
- Zhang C, Feng X-T, Zhou H, Qiu S, Wu W (2012) Case histories of four extremely intense rockbursts in deep tunnels. *Rock Mech Rock Eng* 45(3):275–288
- Zhang X, Chen Z, Liu Y (2016) The material point method: a continuum-based particle method for extreme loading cases. Academic Press, New York
- Zhuang X, Chun J, Zhu H (2014) A comparative study on unfilled and filled crack propagation for rock-like brittle material. *Theor Fract Mech* 72:110–120
- Zubelewicz A, Mroz Z (1983) Numerical simulation of rock burst processes treated as problems of dynamic instability. *Rock Mech Rock Eng* 16(4):253–274

**Publisher's Note** Springer Nature remains neutral with regard to jurisdictional claims in published maps and institutional affiliations.

Springer Nature or its licensor (e.g. a society or other partner) holds exclusive rights to this article under a publishing agreement with the author(s) or other rightsholder(s); author self-archiving of the accepted manuscript version of this article is solely governed by the terms of such publishing agreement and applicable law.